

OBSERVATIONS OF A4059 WITH *CHANDRA*, *HUBBLE SPACE TELESCOPE*, AND THE VERY LARGE ARRAY: UNRAVELING A COMPLEX CLUSTER/RADIO GALAXY INTERACTION

YUN-YOUNG CHOI,^{1,2,3} CHRISTOPHER S. REYNOLDS,⁴ SEBASTIAN HEINZ,⁵ JESSICA L. ROSENBERG,⁶ ERIC S. PERLMAN,⁷ AND JONGMANN YANG^{1,2}
Received 2003 March 28; accepted 2004 January 16

ABSTRACT

We present a detailed reanalysis of *Chandra* data for the galaxy cluster A4059 and its central radio galaxy, PKS 2354–35. We also present new 1.4 and 4.7 GHz CnB-array radio data from the Very Large Array, as well as a short archival WFPC2 image from the *Hubble Space Telescope*. The presence of a strong interaction between this radio galaxy and the intracluster medium (ICM) was suggested by Huang & Sarazin on the basis of a short observation by the High Resolution Imager on *ROSAT* and confirmed in our preliminary analysis of the *Chandra* ACIS-S data. In particular, X-ray imaging clearly shows two cavities within the ICM that are *approximately* aligned with the radio galaxy axis. However, using our new radio maps (which are at lower frequencies and better matched to searching for $\sim 1'$ structures than the previous high-quality maps), we fail to find a detailed correspondence between the $\sim 1'$ scale radio lobes and the ICM cavities. This suggests that the cavities are “ghosts” of a previous burst of powerful activity by PKS 2354–35. This is supported by detailed, spatially resolved X-ray spectroscopy that fails to find any shock-heated ICM, suggesting that the cavities are evolving subsonically. We also examine the nature of the central asymmetric ridge (or bar) of X-ray emission extending for ~ 30 kpc southwest of the cluster center that has been noted in these previous analyses. We find the ridge to be denser and cooler than, but probably in pressure balance with, its surroundings. The thermal evolution of this structure seems to be dominated by radiative cooling, possibly enhanced by the radio galaxy–ICM interaction. We discuss several possible models for the formation of this southwest ridge and find none of them to be entirely satisfactory. In our preferred model, the southwest ridge is due to radiative cooling induced by an interaction between a radio galaxy–driven disturbance and a preexisting bulk ICM flow. The presence of such a bulk flow (with a velocity of ~ 500 km s⁻¹ projected on the plane of the sky) is suggested by the off-center nature of the pair of X-ray cavities. Such a bulk flow can be created during a cluster/subcluster merger—the presence of a prominent dust lane in the cD galaxy of A4059, ESO 349–G010, is circumstantial evidence for just such a merger.

Subject headings: galaxies: clusters: individual (A4059) — galaxies: individual (PKS 2354–350) — galaxies: jets — X-rays: galaxies: clusters

1. INTRODUCTION

There is an increasing realization that the core regions of clusters of galaxies are complex and dynamic environments. For some time now, it has been argued on the basis of data from imaging X-ray telescopes that the hot intracluster medium (ICM) of the core regions of rich clusters is radiatively cooling on timescales shorter than the age of the cluster. This gives rise to the phenomenon known as a cooling flow. Fabian (1994) gives an extensive review of cooling flows up to and including constraints from the *ROSAT* observatory. Prior to the launches of *Chandra* and *XMM-Newton*, the X-ray data strongly argued for the inhomogeneous cooling flow model in which gas in cluster cores cools from X-ray–emitting temperatures down to unobservable temperatures as part of a multiphase ICM over a

spatially distributed region of the cluster core. An obvious mystery, and a strong hint that the real situation is more complex, was the lack of cool gas (including significant star formation) observed at other wavebands.

Not surprisingly, the X-ray view of cluster cores became appreciably more complicated with the launch of *Chandra* and *XMM-Newton*. With the very high dispersions possible using the reflection grating spectrometer on *XMM-Newton*, detailed emission-line spectroscopy of cluster cores became possible for the first time. Using these techniques, observations of A1795 (Tamura et al. 2001) and A1835 (Peterson et al. 2001) both revealed clear evidence for gas cooling from the virial temperature $kT > 4$ keV down to 1–2 keV. In particular, one could isolate and identify the L-shell emission lines of iron corresponding to gas spanning this temperature range. However, very tight upper limits were set on the amount of gas below 1–2 keV, which were in strong disagreement with the standard cooling flow model. In other words, there is evidence for gas cooling from the virial temperature down to 1–2 keV, where it disappears. This result has been generalized to a sample of clusters by Peterson et al. (2003). The explanation for the temperature floor is still far from clear. Strong (i.e., order of magnitude) metallicity inhomogeneities will skew the apparent cooling function such that gas below 1 keV cools extremely rapidly, thereby eluding detection (Fabian et al. 2001). However, it is not known how such inhomogeneities will be formed or maintained. Thermal conduction and the

¹ Department of Physics and CSST, Ewha University, Seoul 120-750, Korea.

² Center for High Energy Physics, Kyungpook National University, Daegu 702-701, Korea.

³ JILA, Campus Box 440, University of Colorado, Boulder, CO 80309.

⁴ Department of Astronomy, University of Maryland, College Park, MD 20742.

⁵ Max-Planck-Institut für Astrophysik, Karl-Schwarzschild-Strasse 1, D-85740 Garching, Germany.

⁶ Center for Astrophysics and Space Astronomy, Campus Box 389, University of Colorado, Boulder, CO 80309.

⁷ Department of Physics, University of Maryland—Baltimore County, 1000 Hilltop Circle, Baltimore, MD 21250.

action of a central radio galaxy may also be important in producing these temperature floors (Fabian, Voigt, & Morris 2002; Voigt et al. 2002; Ruszkowski & Begelman 2002).

In addition to spectral complexity, *Chandra* has revealed that many clusters possess morphological complexities that are thought to arise from the interaction of the ICM with a central radio galaxy. In some cases, the association is clear. For example, Perseus A (Fabian et al. 2000), Hydra A (McNamara et al. 2000; David et al. 2001; Nulsen et al. 2002), A2052 (Blanton et al. 2001), and Cyg A (Smith et al. 2002) all show well-defined cavities in the X-ray-emitting gas that are coincident with the current radio lobes of the central radio galaxy. In these sources, it is clear that the radio lobes have displaced the X-ray-emitting gas producing the observed X-ray/radio anticoincidence.

Chandra has also revealed the presence of ghost cavities, i.e., X-ray cavities that are *not* coincident with the active radio lobes. Examples include the outer cavity of Perseus A (Fabian et al. 2000), A2597 (McNamara et al. 2001), NGC 4636 (Jones et al. 2002), and A4059 (Heinz et al. 2002). In these sources, it is believed that the cavities are associated with old radio lobes (related to previous cycles of active galactic nucleus activity). The low-frequency (74 MHz) synchrotron radio emission expected within this scenario from these old radio lobes has been observed from the ghost cavity of Perseus A (Fabian et al. 2002).

Collectively, these observations give rise to several questions. Most hydrodynamic models for the formation of these cavities (e.g., Clarke, Harris, & Carilli 1997; Heinz, Reynolds, & Begelman 1998; Reynolds, Heinz, & Begelman 2001, 2002, and references therein) involve the pressure-driven growth of a shock-bounded cocoon. However, in almost all cases (with NGC 4636 being a notable exception; Jones et al. 2002), the X-ray shells that bound the observed cavities are cooler than the ambient ICM, seemingly at odds with the shock scenario. It is plausible that the cool shell arises because of the “lifting” of lower entropy material from the cluster core by the radio galaxy activity (Böhringer et al. 1995; Reynolds et al. 2001; Nulsen et al. 2002), but we would still expect to see some fraction of the sources in the shock-bounded phase. More generally, we need to assess the implications of such data for models of radio galaxy evolution. To achieve this goal requires the detailed analysis of more *Chandra* data together with directed numerical simulations.

A4059 was one of the first clusters known to possess X-ray cavities on the basis of data from the *ROSAT* high-resolution imager (Huang & Sarazin 1998). These cavities were approximately coincident with the radio lobes of the FR I radio galaxy PKS 2354–35, which is hosted by the cD galaxy at the center of the cluster. Huang & Sarazin (1998) also noted an interesting barlike feature in the central regions of the cluster perpendicular to the radio axis. The *Chandra* Advanced CCD Imaging Camera (ACIS) observation of this cluster has been previously described by us in Heinz et al. (2002). In that paper, it was shown that the coincidence between the radio lobes and the X-ray cavities is not exact, leading to the conclusion that these are actually ghost cavities. It was also suggested that the complex X-ray morphology (including the central bar) arises from an interaction of a radio galaxy driven expanding cocoon and a preexisting bulk ICM flow. Such an ICM flow may result from the accretion of a galaxy group by the cluster.

In this paper, we present a detailed reanalysis of the *Chandra* ACIS observation of the core regions of A4059. We present a spatially resolved spectral study of the core regions

of this cluster. We also present new 1.4 GHz and 4.7 GHz radio data from the Very Large Array (VLA)⁸ taken with the CnB configuration, thereby providing a better match to the typical spatial scales characterizing the X-ray cavities. We confirm that the arcminute-scale radio lobes indeed do not coincide precisely with the X-ray cavities, especially to the southeast of the center. We also find that the ridge of emission to the southwest of the center is cooler and denser but probably in pressure equilibrium with the surrounding ICM. Furthermore, it is determined that the thermal evolution of this structure must be dominated by radiative cooling. We discuss various models for the southwest ridge, but prefer an explanation in which it corresponds to shock/compression-induced cooling of ICM caused by interaction of the radio galaxy driven disturbance with a bulk ICM flow; however, such a model may suffer fine-tuning problems. Finally, we also present an archival *Hubble Space Telescope* (*HST*) Wide Field Planetary Camera 2 (WFPC2) image of the cD galaxy ESO 349–G010. The presence of a significant dust lane in this elliptical galaxy suggests that it has accreted a gas-rich companion galaxy within the past $\sim 10^8$ yr. This provides further circumstantial evidence for the putative cluster/group merger required to produce the bulk ICM flow. Section 2 details the *Chandra*, VLA, and *HST* data reduction, and § 3 describes our imaging and spectroscopy investigations. The observational results are summarized and possible models discussed in § 4.

Throughout this paper we assume $H_0 = 65 \text{ km s}^{-1} \text{ Mpc}^{-1}$ and $q_0 = 0.5$. Given a redshift of $z = 0.049$, this cosmology places PKS 2354–35 and A4059 at a luminosity distance of 226 Mpc.

2. OBSERVATIONS AND BASIC DATA REDUCTION

2.1. X-Ray Observations (*Chandra*)

A4059 was observed by *Chandra* for 24.6 ks on 2000 September 24 and for 20.1 ks on 2001 January 4, using the ACIS detector. The central radio source, PKS 2354–35, was centered $1'$ from the aim point on the S3 back-illuminated ACIS chip (7), such that the core of the cluster could be imaged entirely by the S3 chip. Here we analyze data from this chip only. The data were filtered so as to include only events with *ASCA* grades 0, 2, 3, 4, and 6. The gain for the first observation was reprocessed using *acis_process_events* with the latest version of the gain file appropriate for data taken with a focal-plane temperature of -120°C (*acisD2000-08-12gainN0003.fits*). Some periods during the first observation were affected by background flares. These were removed by excluding all times for which the background rate exceeded the quiescent rate by a factor of 1.2. This left a total exposure time of 10.1 and 17.7 ks for the two observations, respectively. Using the blank-sky background fields of the same part of the detector, we created a background image and spectrum for each observation. Each background data set was processed using the same gain file in the A4059 observation, and the aspect solutions of each observation were applied to the background data set. All ACIS data reduction was performed using CIAO version 2.2.1, and spectral analysis was performed using the XSPEC fitting package. CIAO version 2.2.1 uses Calibration Database (CALDB) version 2.12.

⁸ The VLA is operated by the National Radio Astronomy Observatory, which is a facility of the National Science Foundation, operated under cooperative agreement by Associated Universities, Inc.

For both imaging and spectral analyses, we did *not* use the overall merged event list for the two observations, since it does not contain a valid aspect solution. This would lead to slight errors in the corresponding exposure maps and insufficient information to build correct response matrix files (RMFs) and ancillary response files (ARFs). Therefore, for imaging analysis, we also generated separate flux-calibrated images for each observation and then combined them to produce a final image. To produce an image giving the integrated flux over the full 0.3–8 keV band, we first computed flux-corrected images in several narrow-energy bands and then summed those flux-calibrated images. This is necessary since the effective area of the telescope is both energy- and position-dependent. To do this, we built several exposure maps that were weighted according to both photoelectric absorption and hot diffuse gas emission models for the incident source spectrum and therefore make it possible to compute the correct surface brightness having less significant spectral variation over the entire image. For spectral analysis, we generated separate source and background spectra (together with the corresponding RMF and ARF files) for each of the two observations and then analyzed them simultaneously. These data reduction steps were facilitated using the CIAO threads provided by the *Chandra* Science Center.

Astrometric information was obtained directly from the aspect solution provided with the *Chandra* data release. There are two sources in the *Chandra* data that can be clearly identified in other data sets that have accurate astrometry. First, the brightest of the small-scale peaks in the centralmost regions of A4059 lie within $0''.5$ of the radio core of PKS 2354–35. Second, a bright X-ray source to the east of the cluster center lies within $1''$ of the Two Micron All Sky Survey source 2MASX J23570418–3448121. Thus, we conclude that the absolute *Chandra* astrometry for this observation is correct to within $1''$.

2.2. Radio Observations (VLA)

The preexisting high-quality radio maps of PKS 2354–35 were taken with the VLA in its A- and B-array configurations at 8.5 and 4.8 GHz (Taylor, Barton, & Ge 1994). Such maps may well miss low surface brightness structure on the arcminute scale, such as could exist within the observed X-ray cavities of A4059. With this motivation, we obtained new VLA data optimized to study structures on the size scale of the X-ray cavities. In detail, we made continuum flux maps of PKS 2354–35 using the VLA-CnB configuration at 6 and 20 cm. We observed PKS 2354–35 for 37 minutes at C band with a 50 MHz bandwidth centered at $\nu = 4.7351$ GHz and for 31 minutes at L band with a 50 MHz bandwidth centered at $\nu = 1.4149$ GHz. PKS 2354–35 is a southern source at $\delta = -34^{\text{h}}45^{\text{m}}30^{\text{s}}$; hence the use of the northern extension, CnB. We were not able to make polarization maps from these data because the restricted time range over which the observations were made meant that no polarization calibrators were available. These VLA data were reduced using standard AIPS methods. The resultant clean beams for natural weighted maps are fairly elongated: the L band (1.4 GHz) beam had a major axis of $20''.3$ and a minor axis of $14''.5$, while the major axis of the C band (4.7 GHz) beam was $6''.2$ and the minor axis was $4''.0$.

2.3. Optical Observations (HST)

The *HST* WFPC2 observed PKS 2354–35 on 2001 April 19 as part of snapshot proposal 8683 (PI: R. van der Marel). The

observations were performed in the F814W (broad *I*) band, and the exposure time was 500 s, split in two to allow the elimination of cosmic rays. The *HST* data were retrieved from the public archive and combined using the IRAF/STSDAS task MKDARK, which also allows the elimination of cosmic rays. The data were then rotated to a north-up orientation using the IRAF task IMLINTRAN and registered using World Coordinate System information in the header. We examined both the high-resolution ($0''.0455$ pixel $^{-1}$) PC image (on which the host galaxy of PKS 2454–35 lies) as well as the four-chip mosaic, which was assembled at $0''.09965$ pixel $^{-1}$ using the IRAF/STSDAS task WMOSAIC.

3. IMAGE ANALYSIS

3.1. X-Ray Morphology

For each of the two *Chandra* observations, the 0.3–8 keV data have been background-subtracted and corrected for detector and vignetting effects using weighted exposure maps (see § 2). The resulting processed images were then combined. Figure 1 shows contours of the adaptively smoothed *Chandra* image overlaid on the optical image (from the Digitized Sky Survey) of the cluster. The adaptively smoothed image was derived by smoothing the raw image with a minimum significance of 4σ using the CIAO tool *csmooth*.

It can be seen that the cluster core has a complex X-ray morphology. The principal morphological features present in these images were previously noted by Huang & Sarazin (1998) and Heinz et al. (2002). The cluster within about $30''$ radius has an hourglass-like structure (or bar) with two broad peaks. The strongest peak, at the center of the cluster, contains further substructure with three bright regions. The brightest region coincides with the optical nucleus (ESO 349–G010 from the Digitized Sky Survey), although it is clearly not a point source. In fact, we do not detect any pointlike source coincident with the nucleus of PKS 2354–35. The second of the principal X-ray peaks is $\sim 15''$ southwest from the center and has no optical or radio counterpart. The southwest edge of

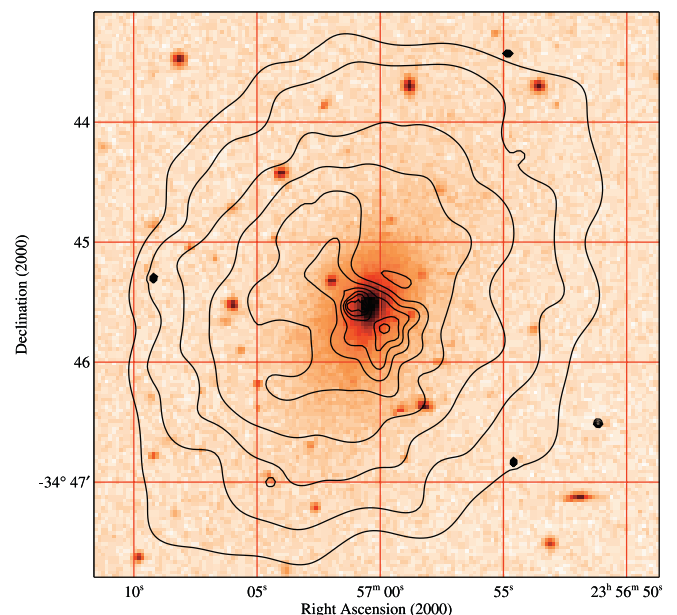


FIG. 1.— 4σ adaptively smoothed ACIS-S image (contours) overlaid on the Digitized Sky Survey image of A4059. See text for discussion.

this feature is so sharp as to be unresolved in our adaptively smoothed map; more precisely, inspection of the smoothing length map produced by *csmooth* indicates that the southwest edge of this feature must be less than $3''$ – $4''$ (3–4 kpc) across. On larger scales, the X-ray emission is elongated and aligned along almost the same position angle as the major axis of the cD galaxy.

Furthermore, there are two cavities in the X-ray emission to the northwest and southeast of the cluster center (see Heinz et al. 2002 for a detailed discussion of the statistical significance of these cavities). The northwest cavity seen in our *Chandra* data can clearly be identified with the northwest cavity seen in the *ROSAT* HRI data. For the more subtle southeast cavity, however, the *Chandra* cavity appears in a different position by about $20''$ from the *ROSAT* HRI cavity. In order to directly compare the *Chandra* image with the *ROSAT* image, we obtained an image in the 0.3–2 keV, which is approximately the band covered by *ROSAT*. This does not change our conclusions regarding the position of the cavity and the discrepancy with *ROSAT*. Considering the unprecedented high spatial resolution and throughput of *Chandra*, we conclude that the southeast cavity given by *Chandra* is likely to be real, not the result of statistical fluctuation (see Heinz et al. 2002). After an examination of the raw *ROSAT* data, we suggest that a 3σ fluctuation in the photon statistics of the *ROSAT* image may have led to an incorrect determination of the southeast cavity's location. We also note that it is difficult to check the correctness of the *ROSAT* HRI aspect solution given the lack of identifiable sources in this short observation.

As pointed out in Heinz et al. (2002), the axis connecting these two cavities lies perpendicular to the central hourglass-like structure, but the center of the axis does not coincide with the radio galaxy (see Fig. 2 in § 3.2). Prompted mainly by that fact, Heinz et al. argued that the radio galaxy had interacted with a moving ICM and, hence, that the cavities had been “blown” in the northeast direction. As we show in § 3.4, spatially resolved X-ray spectroscopy, as well as the *HST* WFPC2 image, provide further support for this hypothesis.

3.2. Radio Morphology

Our new radio maps are presented in Figure 2 as contours of flux density overlaid on an adaptively smoothed 0.3–8.0 keV ACIS image. It is interesting to compare this with the high-resolution 8.5 and 4.8 GHz VLA/A- and B-array images of Taylor et al. (1994). While the radio emission at 8.5 GHz extends to the northwest X-ray cavity and coincides with the deepest part of the cavity, it is not spatially coincident with the southeast cavity (see Fig. 1 in Heinz et al. 2002). Our new CnB-array radio images show that the 1.4 GHz emission also does not extend into the southeast cavity. Indeed, the radio axis does not seem to be aligned with the axis joining two X-ray cavities, and there is no evidence for bending of the radio structure toward the direction of the two cavities. Below we discuss the possibility that the X-ray cavities correspond to old radio lobes that have been moved around by bulk ICM flows and that may only be directly observable at low radio frequencies (100 MHz and below).

3.3. Optical Morphology

Figure 3 shows the *HST* WFPC2 image of the A4059 field. While an analysis of the optical galaxy cluster is beyond the scope of this paper, a large number of bright galaxies can be seen. By far the brightest, however, is the cD galaxy ESO 349–G010, which has been placed on the PC chip. The detailed high-resolution PC image of ESO 349–G010 is shown in Figure 4. The most striking feature is the prominent dust lane that can be traced for at least $5''$ (corresponding to 5 kpc) projected across the central regions of the galaxy. The position angle of the dust lane is twisted by 60° – 70° relative to the radio axis of PKS 2354–35 and coincides with the position angle of the bright southwest ridge in the X-ray image. Similar dust lanes, also oriented roughly perpendicular to the radio axis, have been noted in *HST* data for the host galaxies of three compact symmetric objects (CSOs) by Perlman et al. (2001). The Perlman et al. CSO hosts also possess disturbed outer isophotes that suggest a significant merger

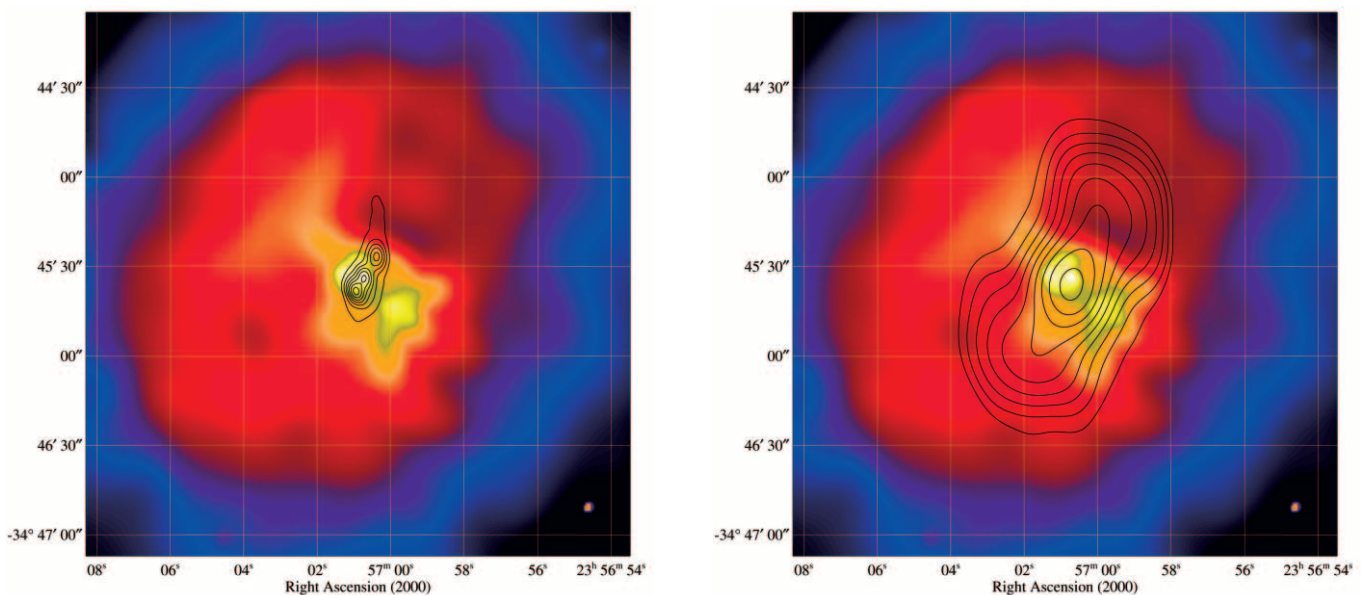


FIG. 2.—VLA/CnB-array images (contours) of A4059/PKS 2354–35 taken at 4.7 GHz (left) and 1.4 GHz (right), overlaid on the 4σ adaptively smoothed X-ray image.

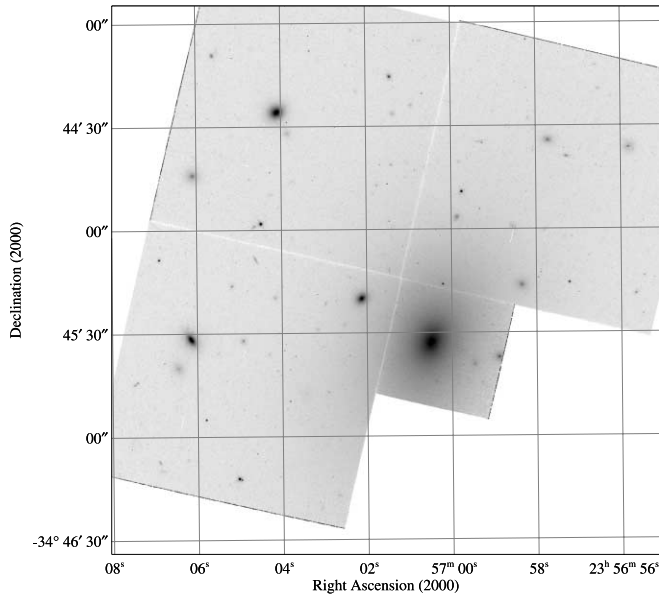


FIG. 3.—*HST* WFPC2 image of the A4059 field (see § 2.3 for details of the observation). The cD galaxy ESO 349–G010 is clearly visible on the PC chip.

event approximately $\sim 10^8$ yr ago. Since it was taken as part of a snapshot campaign, the data for ESO 349–G010 lack the multiband coverage and signal-to-noise ratio (S/N) to perform the Perlman et al. analysis.

3.4. Spatially Resolved X-Ray Spectroscopy

The X-ray morphology of the core of A4059 is complex and asymmetric. Given the obvious lack of spherical symmetry (especially in the central regions of this system), any spatially resolved spectral studies of this cluster will be subject to uncertain projection effects. With these caveats in mind, this section presents a detailed spatially resolved spectroscopic investigation of A4059.

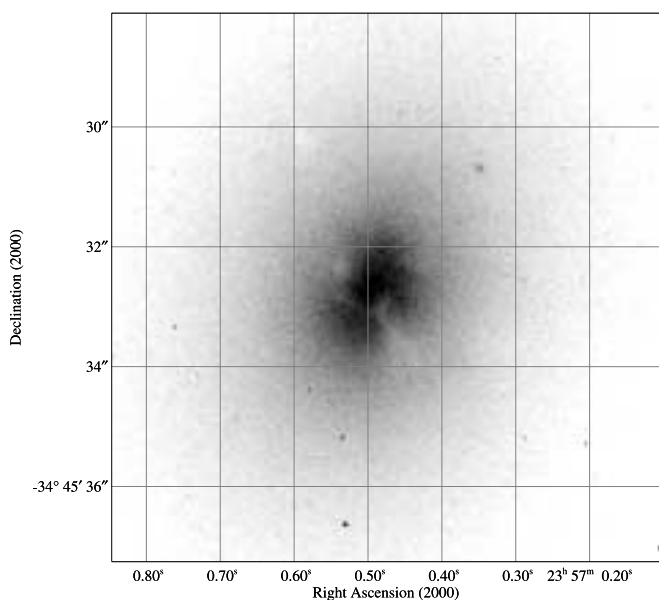


FIG. 4.—WFPC2 imaging of the cD galaxy ESO 349–G010, the host galaxy of the radio source PKS 2354–35 (see § 2.3 for details of the observation). Note the prominent dust lane crossing the galaxy from the northeast to the southwest.

3.4.1. Adaptively Binned Image Analysis

Given the asymmetries present in the cluster core, we must analyze the spectral properties of the cluster across the two-dimensional image. We achieve this using the “adaptive binning” method of Sanders & Fabian (2001). The adaptive binning code, kindly provided by Jeremy Sanders,⁹ computes the optimal tiling across the image such that each tile possesses at least a specified number of photons. Spectra can then be extracted and analyzed for each tile. The major advantage of this method is that one can maintain high spatial resolution (i.e., small tiles) in the high count rate regions of the image.

The adaptive binning was set such that each tile possessed at least 600 counts, resulting in a fractional error on the net count rate of 0.04. Spectra and response matrices were extracted from each tile. Although an analysis using the 0.3–8.0 keV energy range could provide information on cold emission and intrinsic absorption in the cluster, such an analysis is severely hampered by calibration problems at the lowest energies, in particular the effects of contamination on the ACIS filter and charge-transfer inefficiency in the CCD. Therefore, only data between 0.5 and 8.0 keV were included in this spectral analysis. The separate responses for each tile were weighted to account appropriately for instrumental response variations across the detector, using the *mkwarf* and *mkrmf* scripts implemented within CIAO. The original auxiliary response files created by CIAO tool *mkwarf* were corrected for degradation in the ACIS quantum efficiency using the software released by George Chartas and Konstantin Getman.¹⁰ Background spectra were generated using the blank sky fields (Markevitch et al. 2000) for the same part of the detector. All spectra were grouped to have at least 20 photons per energy bin, thereby facilitating the use of χ^2 fitting.

For our canonical spectral fits, each spectrum was modeled with a single-temperature, optically thin thermal plasma component (modeled using the MEKAL model as implemented in XSPEC; Mewe, Gronenschild, & van den Oord 1985; Mewe, Lemen, & van den Oord 1986; Kaastra 1992; Liedahl, Osterheld, & Goldstein 1995) with a metallicity fixed at $Z = 0.4$ and absorbed by the Galactic column density of $N_{\text{H}} = 1.45 \times 10^{20} \text{ cm}^{-2}$. Once we obtained the best-fit plasma emission measure and temperature for each bin, we derived the density, pressure, and cooling time assuming that the plasma is single-phase and has a line-of-sight path length equal to the radial distance between the center of the bin and the center of the cluster (following the method of Fabian et al. 2001). We also studied the effect of relaxing the metallicity constraint and including the possibility of intrinsic absorption.

In Figure 5, we show maps of the best-fitting values of intrinsic absorption (for those fits that relax the absorption constraint), temperature, gas density, metallicity (for those fits that relax the metallicity constraint), pressure, entropy ($s = p/n^{5/3}$), radiative cooling time, and χ^2_{ν} . We have overlaid the X-ray contour map to facilitate comparison. Significant complexity can be seen in these maps. Within the most central regions of the cluster (about $30''$ radius; see dotted circle contour in Fig. 5a), the gas density and pressure dramatically increase, reaching peak values of $n_e \sim 0.11 \text{ cm}^{-3}$ and $p \sim 2.7 \times 10^{-10} \text{ ergs cm}^{-3}$, and the temperature decreases, reaching down to a value of $kT \sim 1.4 \text{ keV}$.

⁹ See <http://www-xray.ast.cam.ac.uk/~jss/adbin>.

¹⁰ See <http://www.astro.psu.edu/users/chartas/xcontdir/xcont.html>.

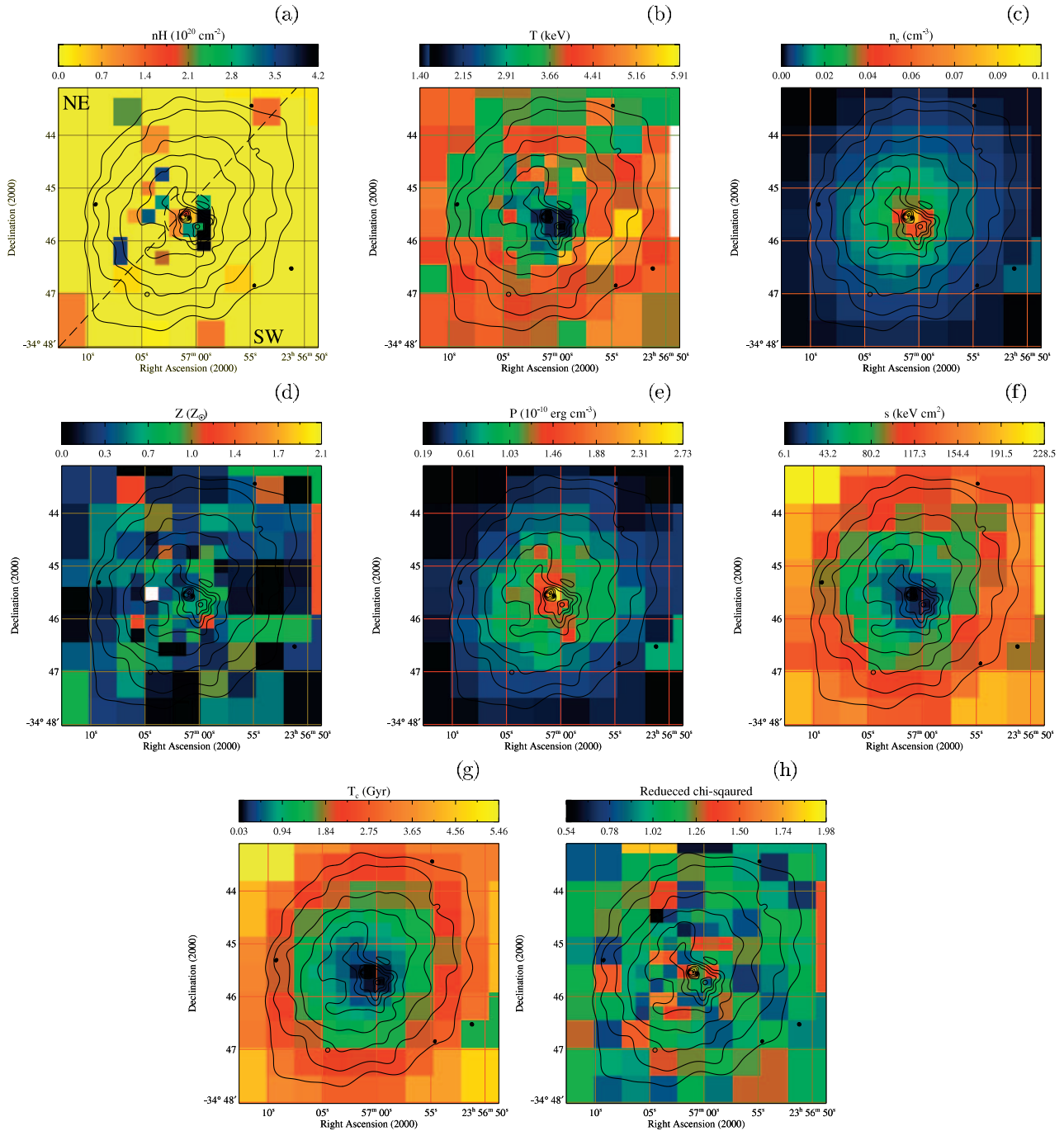


FIG. 5.—Maps of (a) column density, (b) temperature, (c) gas density, (d) metallicity, (e) pressure, (f) specific entropy, (g) cooling time, and (h) the appropriated reduced χ^2 value for adaptively binned central 2.5 image of A4059, with an intrinsic absorption single-temperature MEKAL model. Dotted circle contour ($r < 25$ kpc) includes the bright hourglass-like structured region of the cluster.

One of the most striking and unusual features within the core of A4059 is the bright ridge of emission stretching from the cluster core to the southwest. Our temperature map (Fig. 5b) clearly shows that the ridge is composed of gas that is cool (with a temperature of ~ 1.4 keV) and has low entropy. In order to investigate the spatial differences in the properties of X-ray-emitting gas in and around this structure, Figure 6 shows the best-fitting parameters for the tile fits, averaged in radial bins, as a function of the distance from the center of the cluster. Figure 6 distinguishes between the northeast and southwest sides of the cluster in order to study the nature of the bright southwest ridge. The

most significant result from Figure 6 is that the radiative cooling time within the ridge is rather small (less than 1 Gyr within 25 kpc and about 0.1 Gyr within the innermost few kpc).

The temperature and pressure maps in Figures 5b and 5e exhibit no evidence for any hot gas in or around the cavities. We can see that the southwest part adjacent to the central hourglass-like structure shows obviously sharp gradients in the fitted temperature, entropy, and radiative cooling time maps, while the northeast shows a rather smooth profile. The oscillation of fitted values shown in Figure 6 results from this nonaxisymmetric feature.

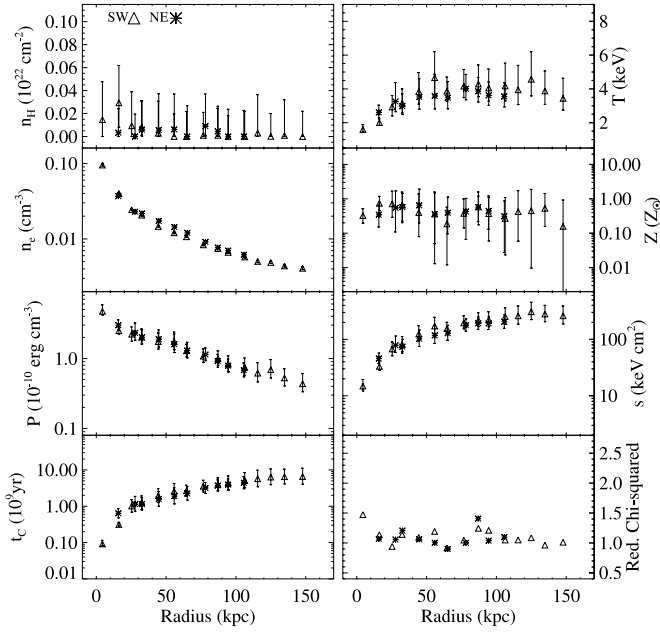


FIG. 6.—Radial distribution of the fitted parameters for the bins in Fig. 5 with 1σ errors. Each profile corresponds to the fitted values of northeast and southwest sides of the cluster center. The radius is the mean distance from the cluster center to each bin.

3.4.2. Detailed X-Ray Spectral Study of Annuli

Motivated by the above analysis, we have examined the spectra for annular regions in the cluster. Source spectra, background spectra, response matrices and ancillary files were generated for each annular region, as in § 3.4.1. Finally, the spectra were binned so as to possess a minimum of 20 counts per bin, thereby allowing the use of χ^2 fitting techniques. We

fitted each spectrum to a variety of models in the energy range of 0.8–8.0 keV:¹¹ a single-phase emission model and two multiphase emission models. For a single-phase emission model (hereafter, model S), the spectrum is fitted with a single-temperature MEKAL model, and for multiphase emission models, the spectrum is fitted with a two-temperature MEKAL model (model T) or a single-temperature plasma plus cooling flow model (model SCF). In the cooling flow model, we set the upper (initial) temperature of the cooling material to be equal to the temperature of the single plasma component. The lower “cutoff” temperature of the cooling flow model is set to 0.1 keV (i.e., significantly below our bandpass). In this analysis, the intervening neutral absorption column density is left as a free parameter. For reference, the Galactic absorption column density is $N_{\text{H,Gal}} = 1.45 \times 10^{20} \text{ cm}^{-2}$.

The results of this analysis are shown in Figure 7, together with the 90% confidence ranges for one interesting degree of freedom ($\Delta\chi^2 = 2.7$). Here we report the results for both the fixed abundance fits (*open squares*) and variable abundance fits (*diagonal crosses*).

When fitted with a single-temperature component plasma model (parameterized by a single temperature and a single emission measure; Fig. 7a), some clear trends are seen. The temperature decreases from 4 keV in the outer regions of the cluster to 2 keV in the central regions. When applying model S with metallicity as a free parameter, we find an enhanced metallicity (approaching almost cosmic abundances) at intermediate radii (20–50 kpc), with metallicities decreasing to 0.4–0.5 Z_{\odot} of the cosmic value at smaller and large radii. The goodness of fit, however, is rather poor when applying model S to the cluster center. Much of the poor goodness of fit is due

¹¹ Note that a more stringent lower limit on the energy band (0.8 keV) is used in this analysis as compared with the adaptive-binning analysis presented above. This is to secure against calibration issues in these higher S/N spectra.

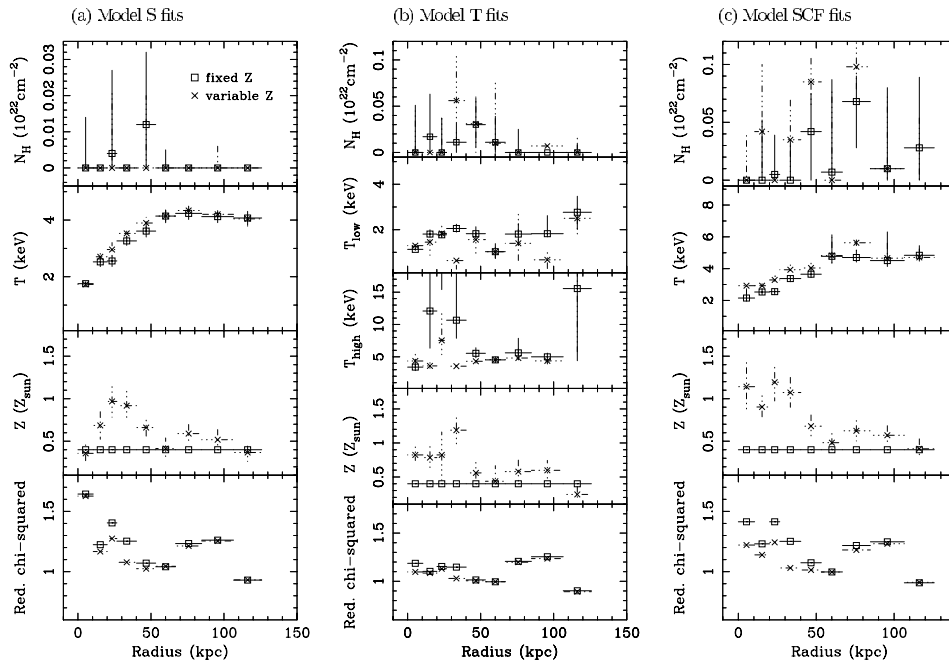


FIG. 7.—(a) Temperature, absorbing column density, metallicity, and the appropriate reduced χ^2 value as a function of radius fitted with the single-temperature MEKAL model (model S). (b) Two-temperature MEKAL model (model T). (c) Single-temperature plasma plus cooling flow model (model SCF). Error bars are shown at the 1σ level for one interesting parameter ($\Delta\chi^2 = 1$). Open squares and crosses show the results with metallicity fixed to the 0.4 times solar value and metallicity-free, respectively. For model T, the metallicities of the two phases were fixed to be same.

to an underprediction of the soft flux by the single-temperature model. It is this mismatch that is responsible for the unphysically small absorption (i.e., less than $N_{\text{H,Gal}}$) implied by these fits.

The two-temperature model (model T; Fig. 7b) is a much better description of the spectral data, especially within the inner 50 kpc. The actual values of the two temperatures seem to be weak functions of radius, with $kT_{\text{high}} \approx 4\text{--}5$ keV and $kT_{\text{low}} \approx 1\text{--}2$ keV in most of the radial bins. Apparent exceptions to this are the 20–40 kpc radial bins that, in the fixed abundance fits, both appear to have $kT_{\text{high}} > 7$ keV. However, variable abundance fits suggest that the abundance strongly deviates from $Z = 0.4 Z_{\odot}$ at these radii, and once that is accounted for, the upper plasma temperature is also approximately 4 keV. The principal qualitative difference between the one- and two-temperature fits lies in the abundance profile. In the one temperature fits, there is a pronounced drop in the metallicity as one proceeds from 30 kpc into the center of the cluster. On the other hand, the two-temperature fits show a jump in the metallicity at about 40 kpc, with the metallicity displaying an approximately flat radial dependence within this radius. Thus, the metallicity peak noted in the single-temperature fits is probably an artifact of the model (also see case of the Virgo Cluster; Molendi & Gastaldello, 2001). Because of the better quality of these fit (especially in the soft band), the measured absorption column is more meaningful for model T. We see that all radii are consistent with Galactic absorption; i.e., there is no evidence for intrinsic absorption in this cluster.

The cooling flow model (model SCF) is a poorer description of these data than the two-temperature model (model T). This is due to the fact that the model includes gas at all temperature from the ambient temperature down to 0.1 keV whereas, as noted in § 1, the cooling in many clusters (including A4059; Peterson et al. 2003) is truncated at 1–2 keV by some process. With this caveat, we note that the cooling flow model reproduces the temperature structure of model S and the metallicity behavior of model T.

3.4.3. Deprojection Analysis

Of course, the analysis presented in the previous section has not attempted to correct for projection effects; the observed emission from a particular annulus contains all of the projected foreground and background emission, thereby complicating the interpretation of these results.

To address this complication, we have performed a spectral analysis of “deprojected” spectra. In detail, we deproject the cluster emission into eight shells assuming spherical symmetry using the *project* model within the XSPEC spectral fitting package.¹² Clearly, any simple symmetry assumption will break down in the morphologically complex inner regions of A4059. However, we might hope to perform a deprojection analysis of this cluster beyond 30–40 kpc, where it is fairly regular.

With this deprojection in hand, we initially model the spectrum of each shell with an absorbed one-temperature MEKAL model in which the global abundance is a free parameter. The density of the plasma is determined from the plasma emission measure assuming that the plasma uniformly fills the volume of the shell. These results are reported in

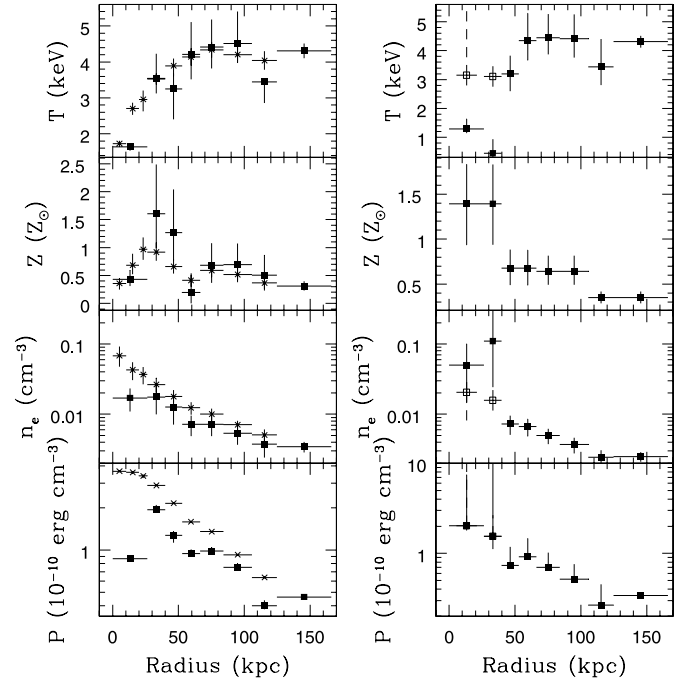


FIG. 8.—Deprojection analysis of the *Chandra* ACIS-S data for A4059. (a) Results of fitting a single-temperature plasma to the spectrum from each shell (*filled squares*), with the density determined from the emission measure assuming that the plasma uniformly fills the volume of the shell. The crosses show the results from the (projected) annular study of § 3.4.2, with the density naively determined from the emission measure. (b) An additional plasma component has been included in the deprojected study in those bins for which it makes a significant improvement to the goodness of fit (i.e., the inner two bins). It is assumed that the two components are in pressure equilibrium, have the same metallicity, and jointly fill the volume of the shell.

Figure 8a; for comparison, we also show the results from fitting model S to the spectra from the projected annuli (naively computing the density from the observed emission measure of the annulus). It can be seen that the single-temperature deprojection study reproduces the peak in metallicity at 30–40 kpc. Within this radius, the spherical assumption clearly breaks down, and hence the deprojection is not to be trusted. Indeed, the leveling off of the ICM density and the drop in ICM pressure within the centralmost bin is unphysical and almost certainly due to the morphological complexities associated with the radio galaxy/ICM interaction.

In order to examine the possibility of multiphase gas, we add an additional temperature component to those deprojected spectra for which it is a significant improvement in the goodness of fit (employing the *F*-test with a 90% level confidence threshold). Only the inner two radial shells required a second temperature component (Fig. 8b). As in the case of the projected study, the central metallicity drop is removed by the addition of a second component.

4. DISCUSSION AND CONCLUSIONS

4.1. Summary of Observational Results

There is clear evidence of a vigorous and complex radio galaxy/cluster interaction between PKS 2354–35 and A4059. Prior to the analysis presented in this paper, the known facts relevant to this interaction were the following:

1. There are two large ICM cavities approximately aligned with the axis of the radio galaxy. Huang & Sarazin (1998) and,

¹² Note that we use the latest version of *project* that can correctly handle the multiple data sets.

later, Heinz et al. (2002) showed that the radio source, as defined in the A- and B-array 4.8 and 8.5 GHz VLA observations of Taylor et al. (1994) extends into the northwest cavity but does not extend to (or even point at) the southeast cavity.

2. There is an offset between the center of the axis connecting the two cavities and the galactic nucleus. One is given the impression that, assuming the cavities were created symmetrically by the radio galaxy, they have subsequently “drifted” in a northeast direction.

3. There is a bright ridge of emission extending from the center of the cluster in the southwest direction. This ridge terminates about 25 kpc to the southwest of the center in an abrupt edge.

To this, we can now add the following information:

1. VLA/CnB-array data taken at 1.4 GHz, which is much better matched to detecting arcminute-scale structures than the previous radio data, still fails to detect any radio emission associated with the southeast X-ray cavity.

2. There is no indication that the gas around the X-ray cavities is any hotter or higher entropy than the ambient gas. In other words, there is no evidence for a strong (or even moderately weak) shock surrounding the X-ray cavities.

3. The southwest ridge appears to be in approximate pressure balance with the ambient material and is X-ray-bright because of its lower temperature and higher density. The radiative cooling time in this structure is much shorter than that of the surrounding ICM, becoming as short as 100 Myr (compared with a general “core” cooling time of greater than 500 Myr).

4. There is a robust metallicity gradient within the cluster, with high metallicity (approaching solar) in the cluster center and then declining by a factor of 2 beyond 50 kpc. This is reproduced in both the annular (i.e., projected) and deprojected spectral study. The presence of a central depression in the metallicity profile is suggested by single-temperature fits to either the projected or deprojected spectra. However, the reality of this feature is unclear (see above for details).

5. *HST*/WFPC-2 imaging reveals that the cD galaxy and host of PKS 2354–35 and ESO 349–G010 displays a prominent 5 kpc dust lane oriented roughly perpendicular to the radio axis. This suggests that it has accreted a dust-rich companion galaxy in the past 10^8 yr or so.

In the following section, we discuss the constraints that these observations place on the nature of the interaction.

4.2. *Inflating the Cavities*

As discussed in Heinz et al. (2002), the current radio source is likely too weak to produce notable cavities, and it is likely that the observed ICM cavities are ghosts of a previous and more powerful period of activity. In this picture, the cavities are in a passive phase of evolution (see Reynolds et al. 2002). The X-ray cavities, which were created by a past phase of supersonic lobe expansion, have decelerated to subsonic velocities. Any shocks once bounding the lobes have weakened into mere compression waves. The fact that this activity produces an expanding shell of ICM implies that gas from the core regions will be lifted to higher points in the cluster, thereby adiabatically cooling as it depressurizes. This cooling effect can largely offset the heating from the ICM compression and (certainly to within the accuracy of our data) mask any remaining signs of compressional heating. This explains the lack of hot gas in or around the cavities.

In this evolutionary phase, the cavities will buoyantly rise within the cluster potential on a timescale a factor of a few longer than the sound crossing time of $\sim 2 \times 10^7$ yr. As they rise buoyantly and expand, the relativistic electron population will undergo synchrotron, inverse Compton, and adiabatic energy losses. The synchrotron and inverse Compton losses result in a high-frequency cutoff that gradually marches to lower and lower radio frequencies. Using the standard formulae for synchrotron losses (e.g., Rybicki & Lightman 1979), it is readily shown that, assuming an isotropic relativistic electron distribution evolving in a constant or decreasing strength magnetic field, the high-frequency cutoff of the synchrotron spectrum will obey

$$\nu_{\text{cut}} \lesssim 26 \left(\frac{B}{60 \mu\text{G}} \right)^{-3} \left(\frac{t}{20 \text{ Myr}} \right)^{-2} \text{ MHz}, \quad (1)$$

where approximate equality corresponds to the case where the magnetic field and the particle pressure are constant in time. This expression assumes no fresh injection or acceleration of relativistic electrons (which would turn the cutoff into a spectral break) and hence only applies once the radio lobes are no longer supplied by active jets (i.e., after the radio source “dies”). The ICM pressure at the location of the ghost cavities is measured to be approximately $p \approx 10^{-10}$ ergs cm^{-3} . If we assume that the synchrotron emitting plasma is in pressure equilibrium with the surrounding ICM (which is very likely to be true for the ghost cavities) and, furthermore, that the magnetic field in the plasma has approximately equipartition strength and is tangled on scales that are small compared to the cavity size, this pressure gives us a field strength of $B \approx 60 \mu\text{G}$. Thus, assuming ICM/cavity pressure balance and equipartition magnetic fields, we can see from equation (1) that the cavities will fade out of the 1.4 GHz band only 4 Myr or so after the outburst of the radio galaxy activity has ceased. Since we believe the ghost cavities to be approximately 20 Myr old (Heinz et al. 2002), we see that there has been ample time for the plasma filling the cavities to fade out of the higher frequency radio bands *if the magnetic field possesses roughly equipartition strength*.

Studies with *ROSAT*, *Chandra*, and *XMM-Newton* have allowed the magnetic field strengths of several radio lobes to be estimated through the direct detection of the X-rays thought to be produced by inverse Compton scattering of the cosmic microwave background by the relativistic electrons (Leahy & Gizani 2001; Hardcastle et al. 2002; Grandi et al. 2003; see also Wilson, Young, & Shopbell 2001 for related arguments in the hot spots of Cyg A). In these studies, it is typically found that the magnetic field is at least a factor of 2 lower than the equipartition value. Even if the magnetic field has half of the equipartition field strength, there is sufficient time for the 1.4 GHz emission from the ghost cavities to fade.

Having put forward a fairly traditional hypothesis for the formation and evolution of the X-ray cavities, we now proceed to consider the complexities special to A4059.

4.3. *Possible Formation Mechanisms for the Southwest Ridge*

One of the most striking feature in the X-ray morphology of A4059 is the bright and cool southwest ridge. The southwest edge of this ridge appears to be a surface across which the temperature and entropy of the gas change significantly with little or no change in pressure. In many ways, this is similar to the “cold fronts” that have been observed in many clusters

(Markevitch et al. 2000; Vikhlinin, Markevitch, & Murray 2001). Here we discuss four possible formation mechanisms for this structure.

4.3.1. A Cool Disk Associated with a Rotating Cooling Flow

Huang & Sarazin (1998), who were the first to note the southwest ridge using *ROSAT* HRI data, suggested that it might be the rotationally supported disk of cooled gas expected to form at the center of a rapidly rotating cooling flow. The notion that such a disklike structure can form in high angular momentum cooling flows has gained support from axisymmetric hydrodynamically simulations (Garasi et al. 1998), although there are still unresolved questions as to the effect that turbulent angular momentum transport may have on the formation and stability of such disks (Nulsen, Stewart, & Fabian 1984).

However, it is clear from the high-resolution *Chandra* ACIS data that the southwest ridge does *not* extend northeast of the cluster center, i.e., it is one-sided. This can be seen in both the total intensity map (Fig. 1) and, more clearly, in the temperature map (Fig. 5b). This runs counter to the idea that the southwest ridge is part of a large (~ 20 kpc) disk at the center of the cluster. Thus, just on the basis of morphology, we can reject the hypothesis that this structure is part of a disk associated with a rotating cooling flow.

4.3.2. Cool Wakes of Buoyantly Rising Radio Plumes

Numerical simulations of the buoyant phase of a radio galaxy evolution show that appreciable amounts of ICM from the cluster core can become entrained in the “wake” of a buoyantly rising plume of radio plasma (Brüggen et al. 2002; Reynolds et al. 2002). This material adiabatically decompresses and cools as it is dragged upward in the cluster potential and would appear as distinct filaments of cold and dense material strung out along the path of the buoyant plume.

As discussed by Young, Wilson, & Mundell (2002), these wakes of cold gas are probably responsible for the arclike feature seen in *ROSAT* HRI and *Chandra* ACIS observations of M87 and the core of the Virgo Cluster. This structure is composed of narrow filaments or columns of cold gas (with $kT \sim 1$ keV, compared with $kT \sim 3$ keV for the surrounding ICM), probably in pressure equilibrium with their surroundings, that extend for $2'-3'$ east and southwest of M87. They are coincident with, but more narrowly confined than, the 90 cm radio arc observed by Owen, Eilek, & Kassim (2000). This supports the idea that the filament has been entrained and pulled out of the central parts of M87/Virgo by a buoyantly rising plume.

However, it seems unlikely that such a model can explain the southwest ridge of A4059. There is no indication of any radio lobe (even a very old one) in the southwest direction; i.e., there is no radio emission and no ICM cavity in that quadrant of the cluster. Furthermore, the southwest ridge does not take on the form of a narrow filament reaching out from the cD galaxy, as would be expected for wake material on the basis of both the numerical simulations and the Young et al. (2002) observations of Virgo. Instead, the southwest ridge is a rather broad and flaring feature extending from the cD galaxy. On the basis of these two observations, we reject the hypothesis that the southwest ridge corresponds to cool material that has been entrained in the wake of a buoyantly rising plume of radio plasma.

4.3.3. The Accreted Core of a Cooler Subcluster

The discovery of a large dust lane in the *HST*-WFPC2 image of ESO 349–G010 suggests the accretion of a dust- and gas-rich companion galaxy within the past 10^8 yr. It is possible that this galactic-merger event was actually the late stages of the merger of a smaller galaxy cluster or group with A4059. In this case, one may attempt to identify the southwest ridge with the remnant ICM core of the minor cluster. The well-known correlation between the X-ray luminosities and temperatures of galaxy clusters and groups, $L \sim T^3$, means that the accreted minor system is likely to possess an ICM that is significantly cooler than the ambient temperature of A4059 ($kT \sim 4$ keV). We note that similar ideas have been proposed to explain the cold fronts observed in other clusters (Markevitch et al. 2000; Bialek, Evrard, & Mohr 2002; Nagai & Kravtsov 2002).

However, this scenario may be problematic for the case of A4059 (although it may well explain some of the classical cold fronts seen in other clusters). While it is true that the ICM temperature of the accreted subcluster may initially be cooler than that of A4059, it will compress and heat as it enters the higher pressure environment of the richer cluster. The relevant thermodynamic quantity to consider is the *entropy* of the ICM cores of A4059 and the accreted cluster. In fact, for clusters of the mass of A4059 and smaller, the entropy of the ICM core is almost constant from one cluster to another (Lloyd-Davies, Ponman, & Cannon 2000; Mushotzky et al. 2043). Thus, even if it evolved adiabatically, the ICM core of the accreted group would be compressionally heated to approximately the ambient temperature of A4059. Any departure from adiabatic evolution (e.g., the effects of shocks) will only increase the entropy and temperature of the accreting ICM. In order to produce a colder region, radiative cooling needs to dominate the evolution of the accreted core. While this may be true, either fine-tuning or significant feedback (either via conduction or radio galaxy heating) is needed to prevent the core from cooling completely.

4.3.4. A Compression Front Associated with Bulk ICM Motion

The apparent displacement of the center of the cavities from the cluster center and the different position angle between the extended radio emission and the cavities suggests bulk motion of the ICM flow. Noting that the line connecting the centers of the two cavities misses the radio galaxy core by approximately $10''$, corresponding to 10 kpc, we can use estimates of the age of the radio source (~ 20 Myr; Heinz et al. 2002) to estimate that the ICM is flowing past the cD galaxy at a velocity of 500 km s^{-1} projected onto the plane of the sky. The different position angle between the axis connecting the ghost cavities and the current extended radio emission demands either a change in the radio axis itself, or some rotation in the ICM flow. Both numerical simulations (e.g., Roettiger, Loken, & Burns 1997) and *Chandra* observations (e.g., Markevitch et al. 2003) suggest this kind of large-scale ICM “sloshing” can readily occur after a major cluster merger.

In this picture, the bright and cool southwest ridge is located at the position where we expect the radio galaxy-induced expanding ICM shell to be maximally compressed by the ICM flow. The sharp southwest edge of this feature is readily interpreted at the interface between the ambient ICM (which we suppose is flowing in a northeast direction) and the expanding ICM shell formed by the same period of radio galaxy activity that formed the X-ray cavities.

One might expect that such compression would heat this material, contrary to observations. However, the fact that the cooling time of the ridge material is small demands that we consider radiative cooling effects. In the simplest case of adiabatic compression in the bremsstrahlung regime, the cooling time is proportional to $n^{-2/3}$. Hence, a weak shock will slightly reduce the cooling timescale. Radiative cooling can be further aided by the kinematics of the radio galaxy/cluster interaction, which keeps this material in the high-pressure regions of the cluster core for longer. Even given this, there appears to be a fine-tuning problem; it is difficult to explain the cooling of the southwest ridge unless it was on the verge of undergoing dramatic radiative cooling anyway. A detailed exploration of

these hydrodynamic and radiative questions will be deferred until future publications.

We thank Mitchell Begelman and Andy Young for stimulating conversations throughout the course of this work. We are also grateful to the anonymous referee for comments that significantly improved the paper. This work was supported by SAO grant GO0-1129X (Y.-Y. C.), the National Science Foundation grant AST 02-05990 (C. S. R.), and Korea Research Foundation grant KRF 2001-041-D00052 (J. Y.).

REFERENCES

- Bialek, J. J., Evrard, A. E., & Mohr, J. J. 2002, *ApJ*, 578, L9
 Blanton, W. L., Sarazin, C. L., McNamara, C. L., & Wise, M. W., 2001, *ApJ*, 558, L15
 Böhringer, H., Nulsen, P. E. J., Braun, R., & Fabian, A. C. 1995, *MNRAS*, 274, L67
 Brügggen, M., Kaiser, C. R., Churazov, E., & Ensslin, T. A. 2002, *MNRAS*, 331, 545
 Clarke, D., Harris, D. E., & Carilli, C. L. 1997, *MNRAS*, 284, 981
 David, L. R., et al. 2001, *ApJ*, 557, 546
 Fabian, A. C., 1994, *ARA&A*, 32, 277
 Fabian, A. C., Mushotzky, R. F., Nulsen, P. E. J., & Peterson, J. R. 2001, *MNRAS*, 321, L20
 Fabian, A. C., Voigt, L. M., & Morris, R. G. 2002, *MNRAS*, 335, L71
 Fabian, A. C., et al. 2000, *MNRAS*, 318, L65
 Garasi, C., Loken, C., Burns, J. O., & Roettiger, K. 1998, *MNRAS*, 298, 697
 Grandi, P., et al. 2003, *ApJ*, 586, 123
 Hardcastle, M. J., Birkinshaw, M., Cameron, R. A., Harris, D. E., Looney, L. W., & Worrall, D. M. 2002, *ApJ*, 581, 948
 Heinz, S., Choi, Y.-Y., Reynolds, C. S., & Begelman, M. C. 2002, *ApJ*, 569, L79
 Heinz, S., Reynolds, C. S., & Begelman, M. C., 1998, *ApJ*, 501, 126
 Huang, Z., & Sarazin, C. L. 1998, *ApJ*, 496, 728
 Jones, C., et al. 2002, *ApJ*, 567, L115
 Kaastra, J. S. 1992, An X-ray Spectral Code for Optically Thin Plasmas (Internal SRON-Leiden Rep., updated ver. 2.0; Leiden: SRON)
 Leahy, J. P., & Gizani, N. A. B. 2001, *ApJ*, 555, 709
 Liedahl, D. A., Osterheld, A. L., & Goldstein, W. H. 1995, *ApJ*, 438, L115
 Lloyd-Davies, E. J., Ponman, T. J., & Cannon, D. B. 2000, *MNRAS*, 315, 689
 Markevitch, M., et al. 2000, *ApJ*, 541, 542
 ———. 2003, *ApJ*, 586, L19
 Mewe, R., Gronenschild, E. H. B. M., & van den Oord, G. H. J. 1985, *A&AS*, 62, 197
 Mewe, R., Lemen, J. R., & van den Oord, G. H. J. 1986, *A&AS*, 65, 511
 McNamara, B. R. et al. 2000, *ApJ*, 534, L135
 ———. 2001, *ApJ*, 562, L149
 Molendi, S., & Gastaldello, F. 2001, *A&A*, 375, L14
 Mushotzky, R. F. 2003, in *AIP Conf. Proc.* 666, Emergence of Cosmic Structure, ed. S. S. Holt & C. S. Reynolds (New York: AIP), 171
 Nagai, D., & Kravtsov, A. 2003, *ApJ*, 587, 514
 Nulsen, P. E. J., David, L. P., McNamara, B. R., Jones, C., Forman, W. R., & Wise, M. 2002, *ApJ*, 568, 163
 Nulsen, P. E. J., Stewart, G. C., & Fabian, A. C. 1984, *MNRAS*, 208, 185
 Owen, F. N., Eilek, J. A., & Kassim, N. E. 2000, *ApJ*, 543, 611
 Perlman, E. S., Stocke, J. T., Conway, J., & Reynolds, C. S. 2001, *AJ*, 122, 536
 Peterson, J. A., et al. 2001, *A&A*, 365, L104
 ———. 2003, *ApJ*, 590, 207
 Reynolds, C. S., Heinz, S., & Begelman, M. C., 2001, *ApJ*, 549, L179
 ———. C., 2002, *MNRAS*, 332, 271
 Roettiger, K., Loken, C., & Burns, J. O. 1997, *ApJS*, 109, 307
 Ruszkowski, M., & Begelman, M. C. 2002, *ApJ*, 581, 223
 Rybicki, G. B., & Lightman, A. P. 1979, *Radiative Processes in Astrophysics* (New York: Wiley)
 Sanders, J. S., & Fabian, A. C. 2001, *MNRAS*, 325, 178
 Smith, D. A., Wilson, A. S., Arnaud, K. A., Terashima, Y., & Young, A. J. 2002, *ApJ*, 564, 176
 Tamura, T., et al. 2001, *A&A*, 365, L87
 Taylor, G. B., Barton, E. J., & Ge, J. P. 1994, *AJ*, 107, 1942
 Vikhlinin, A., Markevitch, M., & Murray, S. S. 2001, *ApJ*, 549, L47
 Voigt, L. M., Schmidt, R. W., Fabian, A. C., Allen, S. W., & Johnstone, R. M. 2002, *MNRAS*, 335, L7
 Wilson, A. S., Young, A. J., & Shopbell, P. L. 2001, *ApJ*, 547, 740
 Young, A. J., Wilson, A. S., & Mundell, C. G. 2002, *ApJ*, 579, 560